



# **AIAA 2000-4218**

## **CFD VALIDATION OF HIGH-LIFT FLOWS WITH SIGNIFICANT WIND-TUNNEL EFFECTS**

**Stuart E. Rogers and Karlin Roth**  
NASA Ames Research Center  
Moffett Field, California

**Steven M. Nash**  
MCAT, Inc., NASA Ames Research Center  
Moffett Field, California

**18th AIAA Applied Aerodynamics  
Conference**  
**14 - 17 August 2000 / Denver, Colorado**

# CFD VALIDATION OF HIGH-LIFT FLOWS WITH SIGNIFICANT WIND-TUNNEL EFFECTS

Stuart E. Rogers\* and Karlin Roth†

NASA Ames Research Center  
Moffett Field, California

Steven M. Nash ‡

MCAT, Inc., NASA Ames Research Center  
Moffett Field, California

## Abstract

The modeling requirements for validating Navier-Stokes computations of a high-lift trapezoidal wing are investigated. This wing has a full-span slat and a full-span flap, and has been tested extensively in the NASA Langley 14- by 22-Foot Wind Tunnel and the NASA Ames 12-Foot Pressure Wind Tunnel. Due to the size of the wing, there are significant facility effects in the data from the 12-Foot wind tunnel. Computational models of the test facility of differing fidelity are developed and tested. Results are compared with experimental lift, drag, surface pressures, and velocity profiles. In the computations, a simplified, inviscid model of the test-section performs as well as a high-fidelity, viscous test-section model. Computed results generally compare very well with experimental data at all but the highest angles of attack. A comparison of computational results from both free-air and wind-tunnel simulations at the same lift condition indicates that it is necessary to simulate the wind-tunnel to perform validation using the 12-Foot experimental data. A subsequent grid-refinement study found that enhanced spanwise resolution increased the accuracy of the computed surface pressures at high-angle of attack, and resulted in a computed maximum lift that was 5% above the experimental value.

## Introduction

Validation of Computational Fluid Dynamics (CFD) software is a very important part of its development cycle. It is also an on-going process for the life of the software. A general-purpose CFD solver

can be used for a wide range of fluid-flow problems. Validation of the solver for a simple problem, such as attached flow over an airfoil, does not validate the software for a difficult problem, such as the flow over a complete aircraft. Thus, responsible use of the software for solving a new class of flow problems requires validation. This work is part of a validation effort for the flow over complex high-lift configurations using an overset grid approach<sup>1-3</sup> and the OVERFLOW solver.<sup>4,5</sup>

Calculating the viscous fluid flow over high-lift configurations challenges CFD. Even in two-dimensions, state-of-the-art CFD codes fail to consistently predict, with sufficient accuracy, trends with Reynolds number or trends with flap/slat rigging changes.<sup>6</sup> The difficulties in simulating high-lift flows come from the severe complexity of both the geometry and the flow field physics. In particular, the wing has multiple elements with very small gaps between them, leading to an interaction of various viscous flow phenomena.<sup>7</sup> Since the fluid dynamics are dominated by viscous effects, only a high-fidelity simulation using the Navier-Stokes equations can provide the accuracy necessary to assist in aircraft design.

Only a limited amount of validation has been performed in the past for three-dimensional (3D) high-lift flows. Some of the reasons given by Bussoletti *et al.*<sup>8</sup> for the lack of such validations include: a lack of sufficient 3D experimental high-lift data; only a limited number of 3D high-lift simulations had been conducted, and the available simulations had been done on relatively simple geometries; such simulations required significant computational and labor resources; and most viscous computational approaches were not able to simulate the complex geometries found on an aircraft configured for high lift.

Previous high-lift CFD simulations and validation in 3D include: Mathias *et al.*<sup>9</sup> and Jones *et al.*<sup>10</sup>, who studied a simple wing with a half-span flap; Cao *et al.*<sup>11</sup> who computed flow over a simplified Boeing

\*Aerospace Engineer.

†Chief, Aerospace Operations Modeling Office. Senior Member AIAA.

‡Research Engineer.

Copyright © 2000 by the American Institute of Aeronautics and Astronautics, Inc. No copyright is asserted in the United States under Title 17, U.S. Code. The U.S. Government has a royalty-free license to exercise all rights under the copyright claimed herein for Governmental Purposes. All other rights are reserved by the copyright owner.

747 high-lift configuration; Mavriplis,<sup>12,13</sup> and Nash and Rogers,<sup>14</sup> who computed flow over the same high-lift trapezoidal wing used in the current work. Some work performed during the same time period as the present work on some complete high-lift aircraft simulations is reported by Slotnick *et al.*,<sup>15</sup> and by Rogers *et al.*<sup>16</sup> In all of these works, the validation was limited to comparisons with experimental forces and pressure coefficients. In some of these works,<sup>9,15</sup> the high-lift configurations were simulated within the wind tunnel, whereas in the others, the configurations were simulated only in free-air.

High-lift configurations generate more lift than cruise configurations, and they experience maximum lift at much higher angles of attack. Because of this, the wall-interference corrections for experimental data acquired for high-lift configurations can be large. The present study compares OVERFLOW simulations of the flow over a trapezoidal high-lift wing (trap wing) with recently acquired experimental data.<sup>17</sup> This wing has been tested in both the NASA Langley 14- by 22-Foot Wind Tunnel (14x22) and the NASA Ames 12-Foot Pressure Wind Tunnel (12-Foot). The blockage area for the trap wing at 26 degrees angle of attack in the 12-Foot test section is 10% of the test-section area. Further, for this configuration, interference correction methods indicate a change of over six degrees in angle of attack due to the 12-Foot facility walls. Thus, the primary goal of the current work is to determine if it is necessary to model the wind-tunnel walls in order to use the 12-Foot data for CFD validation of flow over the trap wing.

Numerous authors have reported on efforts to simulate wind-tunnel facilities in their CFD calculations. Much of the research in this area has focused on developing boundary conditions to simulate porous or slotted wind-tunnel walls, examples of which are given in Refs. 18-21. While much of this work was focused on airfoils in transonic flows with relatively small blockage, the current issues are more concerned with large blockage in a 3D semi-span testing environment. Of interest to high-lift is the work by Cao *et al.*,<sup>22</sup> who studied the effects of upper and lower wind-tunnel walls while computing a high-lift airfoil configuration. They investigated the use of both inviscid and viscous boundary conditions on the walls, and found very little difference between the two. They reported non-negligible interference effects when comparing the wind-tunnel wall computations with free-air computations. A direct predecessor to the current work is that of Dhjomeri,<sup>23</sup> who performed a preliminary investigation of computing flow through the 12-Foot wind-tunnel, using both viscous and inviscid surfaces to model the wind tunnel.

In the following sections, details of the trap-wing geometry used in this study are presented. Following this is a presentation of the computational grids

which were generated for this work, including both a viscous-surface, high-fidelity representation of the 12-Foot, as well as a simplified model of the test section. The computed results are presented, including detailed comparisons between the computed and experimental data, and an analysis of the wind-tunnel interference. Finally, results of computations from a grid system with refined spanwise spacing are presented.



**Fig. 1. Trap wing in the 12-Foot test section.**

## Trap-Wing and Wind-Tunnel Geometries

### Experimental Model

Recent experimental work on a high-lift trap-wing configuration<sup>17</sup> was motivated by the need to produce data which could be used to validate CFD methods for 3D high-lift flows. This trap-wing configuration is a semi-span model and consists of a body pod, a wing, a full-span slat, and either a full-span or a part-span flap. The current work focuses on the full-span flap configuration. The model has been tested in both the 14x22 and the 12-Foot. The 12-Foot data was taken at Reynolds numbers, based on mean aerodynamic chord, ( $Re_c$ ) from 3.4 million to 14.7 million (1 to 4.3 atmospheres), with a Mach number of 0.15; the 14x22 data was taken at  $Re_c = 4.3$  million and a Mach number of 0.2. The data taken in the 12-Foot included: forces and moments; surface pressures; off-body and wake velocity profiles measured with a 7-hole probe; transition measurements using temperature sensitive paint;

mini-tuft surface flow visualization; and wind-tunnel wall pressures. The mean aerodynamic chord ( $c$ ) of the model was 39.6 inches, and the model semi-span was 85 inches. All of the current computed results were obtained for trap-wing landing configuration number one, which had slat and flap deflections of 30 and 25 degrees, respectively, a slat gap of  $0.015c$ , slat overhang of  $0.015c$ , a flap gap of  $0.015c$ , and a flap overhang of  $0.005c$ . In the 12-Foot, the model was mounted on a splitter plate above the floor of the wind tunnel, as seen in Fig. 1.

### Wind-Tunnel Interference

Some initial CFD results for this geometry have been compared to the lower Reynolds-number data from the 14x22 in a previous work by the current authors.<sup>14</sup> These results compared very well with the 14x22 experimental data: the computed lift coefficient (CL) varied from the experimental data by no more than 1.5% from a low angle of attack ( $\alpha$ ) through maximum lift coefficient ( $CL_{max}$ ). Figure 2 is a plot of CL versus  $\alpha$  comparing the 12-Foot,  $Re_c = 5.9$  million, Mach = 0.15, corrected and uncorrected data, with the 14x22,  $Re_c = 4.3$  million, Mach = 0.2 corrected data. Also included in Fig. 2 are previously computed CFD results<sup>14</sup> which were run at the 14x22 flow conditions and using free-air boundary conditions. This shows that the blockage in the 12-Foot is very high, with a shift of up to 6 degrees in angle of attack between the corrected and uncorrected CL.

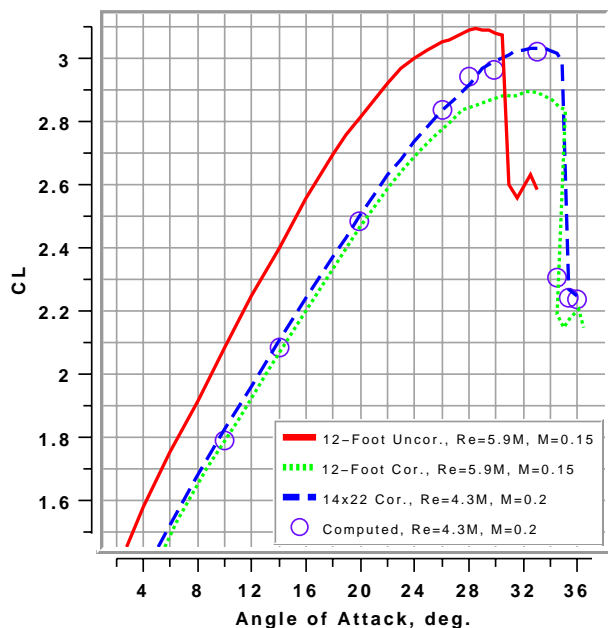


Fig. 2. CL versus  $\alpha$  comparing 12-Foot and 14x22 data.

Since the 14x22 test section is considerably larger than the 12-Foot, the corrections to the 14x22 data are much smaller. This is supported by the excellent

agreement between the 14x22 data and the free-air CFD results. Although the corrected data from the two wind tunnels agree fairly well at the lower angles of attack, the corrected 12-Foot  $CL_{max}$  is considerably lower. The higher Reynolds number and the lower Mach number of the 12-Foot data should both tend to produce higher  $CL_{max}$  values. Thus the difference in the  $CL_{max}$  values is likely due to a difference between the two facilities. The conclusion drawn from Fig. 2 is that any CFD comparisons with the 12-Foot trap-wing data should simulate the effects of the test-section, and should be validated with the uncorrected data. This conclusion is echoed very strongly by the experimental investigators.<sup>17</sup>

### Computational Model

The computational model of the trap wing includes all components of the experimental model except the slat and flap brackets, which hold these elements onto the wing. The grid generation starts with the geometry as defined in CAD files supplied by the trap-wing experimental-design team. The trap-wing grid system is generated utilizing the Chimera Grid Tools (CGT)<sup>24</sup> which includes a series of general-purpose scripts, enabling rapid grid generation and configuration control.<sup>3</sup> The inboard ends of the slat, wing, and flap are sealed against the body pod using collar grids<sup>25</sup> at the intersections. At the tips of these three elements, wingcap grids<sup>2</sup> are used. Figure 3 shows these wingcap surface grids, with only every other grid line plotted.

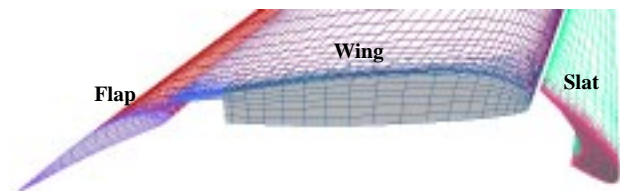


Fig. 3. Wingcap grids on slat, wing, and flap.

In the current work, the 12-Foot test section was modeled computationally using two different approaches. The first of these was a high-fidelity model which included all components present in the 12-Foot test section. This included: a horizontal splitter plate above the tunnel floor on which the model is mounted; a large center fairing underneath the splitter plate; and four hinge fairings at the under-side trailing edge of the splitter plate. The definition of the walls included the slight divergence of the test-section to accommodate the boundary-layer growth. The complete model treated all of the solid surfaces as no-slip, viscous surfaces, and this model is referred to as the “viscous tunnel.”

To mount the trap-wing in the viscous tunnel, the body pod was given a one inch stand-off above the splitter plate. This stand-off distance was sealed with

a viscous collar grid grown onto both the body pod and the splitter plate. In the experiment, a labyrinth seal was used with about a one inch stand-off height.

In the viscous tunnel, the inflow region upstream of the test section included only part of the bell-mouth from the actual tunnel. The computational inflow region was built from a constant-area, circular cross-section which was faired into the downstream section of the actual bell-mouth. This was done to reduce the inflow cross-section area and thus avoid computing an inflow region with very small-magnitude velocities. The outflow region of the computational domain was built by blending together a constant-area cross-section with the actual tunnel geometry, starting about 200 inches downstream of the trailing-edge of the splitter plate. If the actual wind-tunnel outflow expansion was used, it was found that the wakes generated by the high-lift test articles and the wind-tunnel wall boundary layer would separate and become unsteady through the adverse-pressure gradient of the expansion. This unsteady separation would affect the entire flow-field, which would never converge to a steady-state. The use of a constant-area outflow section eliminated this behavior.

The surfaces of the viscous-tunnel grid system are shown in Fig. 4, which plots only every fourth grid line. This complete test-section model adds over 8.3 million grid points to the trap-wing grid system. With this viscous model of the 12-Foot, the entire trap-wing grid system consists of 14.4 million grid points, and 36 zones.

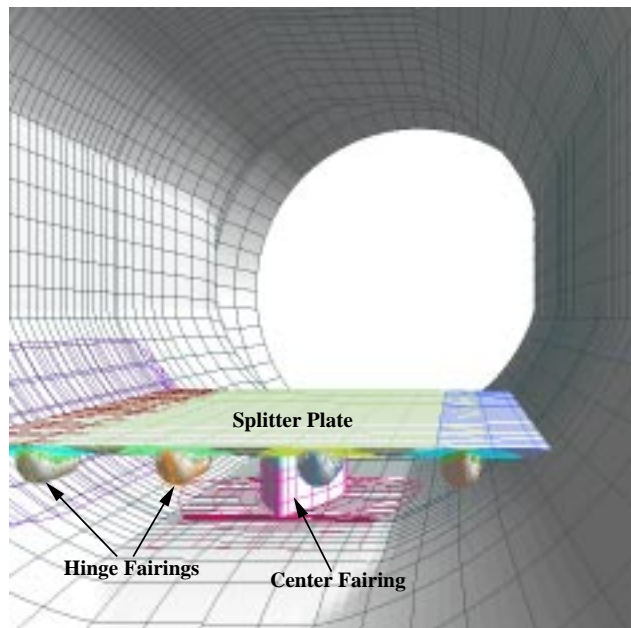


**Fig. 4. Complete computational model of 12-Foot test section.**

Because of the cost of using such a high-fidelity representation of the test-section, a simpler computational model was also developed. This model consisted

of a constant cross-section tube, whose surfaces were treated with inviscid boundary conditions. The cross-section of the tube matched only the cross-section of the actual test section above the splitter plate at the model reference location. This model of the test section was generated using two zones, and required 1.2 million grid points. Utilizing this inviscid model of the 12-Foot, the entire grid system for the trap wing was composed of 14 zones and 6.8 million grid points. Figure 5 shows the surface grids on the entire configuration inside the inviscid wind-tunnel grid, mounted at 26 degrees angle of attack. For clarity, only every fourth grid point in each computational direction is plotted in Fig. 5.

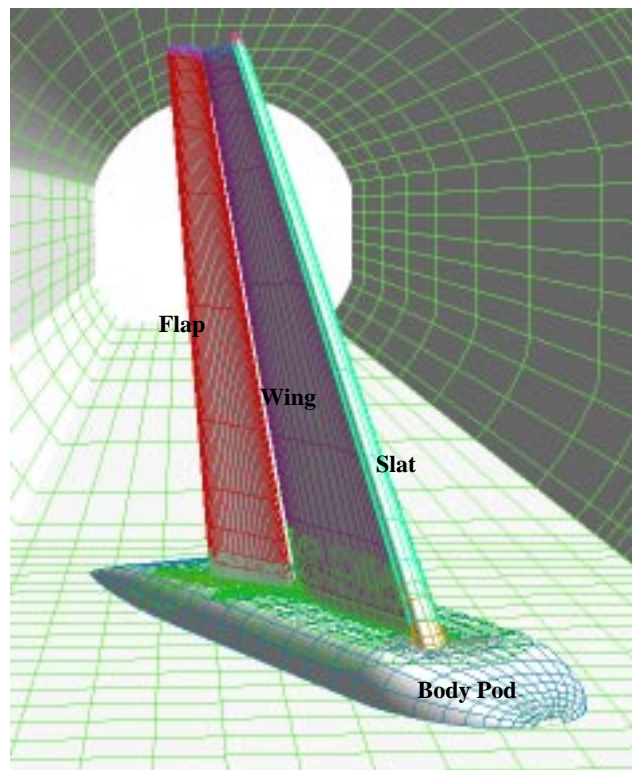


**Fig. 5. Trap wing surface grids inside simplified model of the 12-Foot.**

In addition to the two wind-tunnel grid systems, a free-air grid system was generated by utilizing several Cartesian grids which extended to the far field. The entire free-air grid system contains 6.0 million grid points and 15 zones.

When a model of the wind-tunnel walls was included in the computations, the grid system had to be regenerated for each angle of attack. This was a straightforward task with the overset grid approach. This process started by generating all of the body-fitted volume grids attached to the trap-wing components. These same trap-wing grids are used for both wind-tunnel models and for the free-air calculations. These grids were combined with the wind-tunnel grids for a given angle of attack by rotating and translating the wind-tunnel grids into the coordinate system of the

trap wing. Use of the same coordinate system for all angles of attack simplified the post-processing of the computed solutions.

### Wind-Tunnel Boundary Conditions

One of the biggest challenges of using the viscous wind-tunnel model was determining the appropriate boundary conditions for the tunnel inflow and outflow which would reproduce the same Reynolds and Mach numbers as the experiment. For the inviscid model, this was straight-forward: at the inflow boundary, the total pressure and total temperature were specified to match the experimental values, and the other flow quantities were extrapolated from the neighboring downstream plane; at the outflow boundary, the velocity magnitude was specified to match the mass-flow rate from the experiment, and pressure and density were extrapolated from upstream. This reproduced the same Mach and Reynolds number conditions as in the experiment.

The viscous model of the test section utilized the same total pressure and total temperature inflow conditions as the inviscid model. The boundary layer on the wind-tunnel walls in the viscous model precluded the use of a constant uniform velocity at the outflow. Another method was needed to control the mass flow through the tunnel. An empty, viscous-tunnel grid system was used to develop an appropriate outflow boundary. This grid system was composed of the same viscous wind-tunnel grids but without the trap-wing grids embedded within the test section. Utilizing an outflow boundary condition which specified the static pressure, and extrapolated the other flow quantities, it was found that the mass-flow could be adjusted by changing the value for the outflow static pressure. However, the appropriate value to use was not known a priori, as it was a function of the viscous losses in the wind-tunnel and the drag force on the test article. In addition, much like in a real wind-tunnel, it had to be determined how to sample the computed flow-field to evaluate the effective free-stream reference conditions with the trap wing in place.

This issue was solved using an a procedure analogous to the control system inside the 12-Foot in a semi-span testing mode. This approach interpolates flow quantities from the flow field at six locations. Four of these are known as the Q-ring in the 12-Foot, and are located upstream of the test section, 128 inches upstream of the leading-edge of the splitter plate. Two more probes sample the flow underneath the splitter plate, 46 inches downstream of its leading edge. The Mach numbers at these probe locations are used in a formula to compute the reference Mach number. The formula is based on the cross-sectional areas of the tunnel at the Q-ring, below the splitter plate, and above the splitter plate. The formula used in the CFD

was generated by integrating these areas from the actual CFD grid surfaces, and was adjusted slightly with some calibration computations. The formula is:

$$M_{ref} = 1.120 * M_q + 0.0985 * M_{sp}$$

where  $M_q$  is the average of the Mach numbers at the four Q-ring locations, and where  $M_{sp}$  is the average of the Mach numbers at the two locations beneath the splitter plate. The calibration was performed by running the viscous-tunnel-only grid system for a number of different outflow static pressure ratios. The results of these calibration runs are plotted in Fig. 6. This figure plots  $M_q$ ,  $M_{sp}$ , and the Mach number at the actual model reference location. It compares these with the reference Mach number computed with the above formula. As can be seen in Fig. 6, the measured and computed reference Mach numbers agree very well.

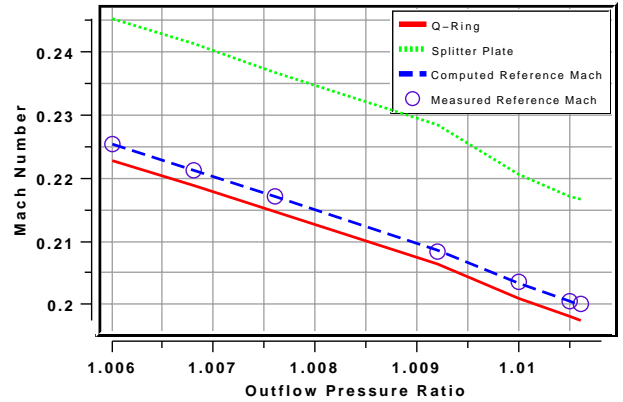


Fig. 6. Mach number versus outflow pressure.

Thus, in order to compute a flow solution using the viscous model of the 12-Foot test section, the outflow static pressure must be iteratively adjusted until the desired reference Mach number has been obtained. In practice, the code was run for approximately 1000 cycles, until the mass flow through the tunnel had nearly converged. Then the reference Mach number was computed, and the outflow pressure boundary condition was adjusted. The code was then run for several hundred cycles until the rate of mass-flow had once again nearly converged, and the adjustment was repeated. As seen in Fig. 6, the rate of change of Mach number with the outflow pressure is nearly linear within this low-speed range, and this process converged quickly. In practice, only four or five adjustments were needed to obtain the desired reference Mach number.

Some pressure-coefficient results from the empty viscous tunnel calibration calculation are plotted in Fig. 7. This shows the pressure coefficient along an axial line 24 inches below the centerline of the tunnel. The experimental results were obtained during 12-Foot calibration tests using a suspended static pipe, with the semi-span splitter plate and fairings installed. The experiment and calculations were run for a reference



Mach number of 0.2 and a Reynolds number of 8 million per foot. The splitter plate leading-edge is located at  $x=1300$  inches, and the trailing edge is located at  $x=1570$  inches. Figure 7 shows that there is very little variation in the pressure along the 22-foot long plate, although the experimental result does show more acceleration at the plate leading edge than the computation, and a slight deceleration through the middle of the test section. Figure 8 shows three boundary-layer profiles from both the computations and the experiment, above the splitter plate located at  $x=1376$ , 1448, and 1532 inches. The model reference location is at  $x=1448$  inches. Good agreement is seen between the computed and experimental boundary layers, and the velocity profiles show more evidence of a slight deceleration in the experimental results.

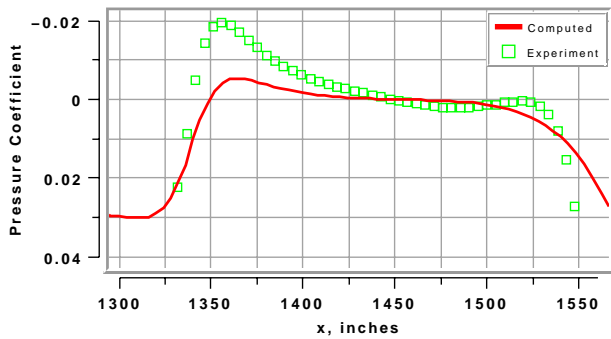


Fig. 7.  $C_p$  along the axis of the tunnel.

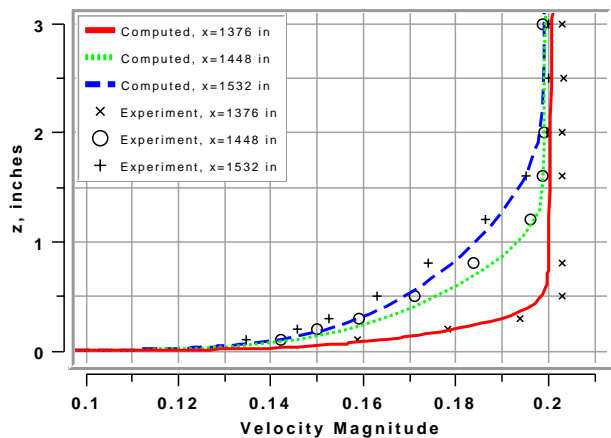


Fig. 8. Splitter-plate boundary layer in empty tunnel.

## Trap Wing Flow Simulation and Analysis

### Flow Solver

The OVERFLOW<sup>4,5</sup> Navier-Stokes flow solver was used in all of the current computations. This code is written to be efficient for computing very large-scale CFD problems on a wide range of supercomputer architectures. On vector supercomputers with very fast

secondary memory devices, the OVERFLOW code includes an out-of-core memory management option, such that the total memory used is a function of the largest zone in the grid system, not the total number of grid points. The code is efficiently vectorized, and its multi-tasking directives take advantage of multiple processors. For cache-based multiple-processor machines, the code has been parallelized with both a multi-level parallelism (MLP) library for shared memory systems, and with a Message-Passing Interface (MPI) library for non-shared memory systems. See Taft<sup>26</sup> and Jespersen<sup>27</sup> for more details. Most of current cases were run with the standard OVERFLOW on a number of different single- and dual-processor Silicon Graphics Octane workstations, over a period of several weeks. Different angle-of-attack runs were run simultaneously on separate workstations. The code was run mostly during non-working hours, utilizing computer resources which would otherwise have gone idle. The viscous-tunnel grid cases were too large to run on the Octane workstations; these cases were run on a Silicon Graphics Origin cluster at NASA Ames.

All of the OVERFLOW computations in the current work utilized the third-order Roe upwind-differencing<sup>28</sup> option, and the Spalart-Allmaras turbulence model<sup>29</sup> with the flow assumed to be fully-turbulent. The viscous terms in all three directions are computed, however the cross-derivative viscous terms were not included. These were not used because they add about 10% to the cost of the computation, and because previous test cases have shown that their use does not affect the solution. The multi-grid option<sup>5</sup> to the code was used with three levels. The current calculations also used the low-Mach number preconditioning option<sup>5</sup> in the flow solver. The code was considered converged to a steady-state when the L2 norm of the right-hand side had dropped at least 2 or 3 orders of magnitude for each computational grid, and when the variation in the total lift coefficient was less than 0.01% over the last 100 cycles. Most cases required between 3000 and 6000 cycles to reach this convergence criteria, and used between 360 to 720 hours of SGI Octane CPU time for each of the inviscid wind-tunnel and free-air cases. The viscous wind-tunnel cases, which had twice as many grid points, required twice as much computer time per case.

### Computed Results

The simulation conditions for the current analysis had a free-stream Mach number of 0.15, a total pressure of 4.3 atmospheres and  $Re_c = 14.7$  million. The viscous wind-tunnel grid system was run for only two cases: 20 and 26 degrees angle of attack. The inviscid wind-tunnel grids were run for ten different angles of attack, ranging from -4 to 28 degrees. Ten different angle of attack cases were run using free-air boundary conditions, ranging from -4 to 32 degrees. Figure 9

shows  $CL$  versus  $\alpha$  for these computed results and for the corrected and uncorrected 12-Foot experimental data. Figure 10 plots the drag coefficient ( $CD$ ) versus  $CL$  for these same cases. These figures show that the viscous and inviscid grid systems produce the same lift and drag at 20 and 26 degrees angle of attack. Also, it can be seen that both the wind-tunnel and free-air calculations agree very well with the uncorrected and the corrected experimental data at the lower angles of attack. Both the wind-tunnel and free-air computations predict  $CL_{max}$  3% lower than the corresponding experimental data. The predictions of the free-air model appear to agree with the corrected data as well as the wind-tunnel cases do with the uncorrected experimental data.

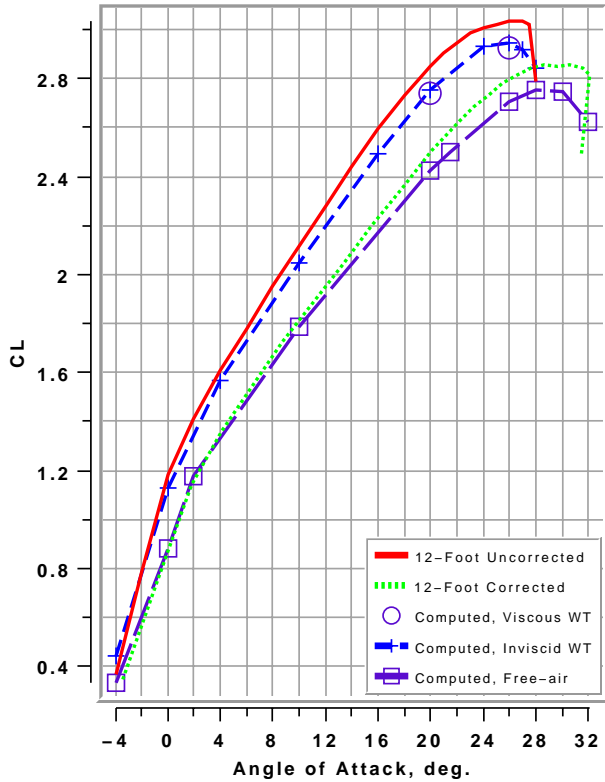


Fig. 9.  $CL$  versus  $\alpha$ .

Figure 11 shows an image of the computational geometry and the locations from which pressure and velocity data have been extracted for comparison with experimental data. Denoted are the nine constant-span planes where the surface pressure coefficients have been extracted. The heavy black lines denote the four flap surface-normal vectors where velocity magnitude data has been interpolated, labeled as profiles 1, 2, 3, and 4. These surface-normal lines are located in the 50% (profiles 1 and 2) and 85% (profiles 3 and 4) spanwise planes, at flap chord-wise locations of 30% and 90% of local chord. These locations correspond to the approximate locations where experimental velocity measurements were taken with a 7-hole probe; however the exact location of the experimental measurements

is not known at this time, and cannot be determined until further post-processing of the experimental data takes place.

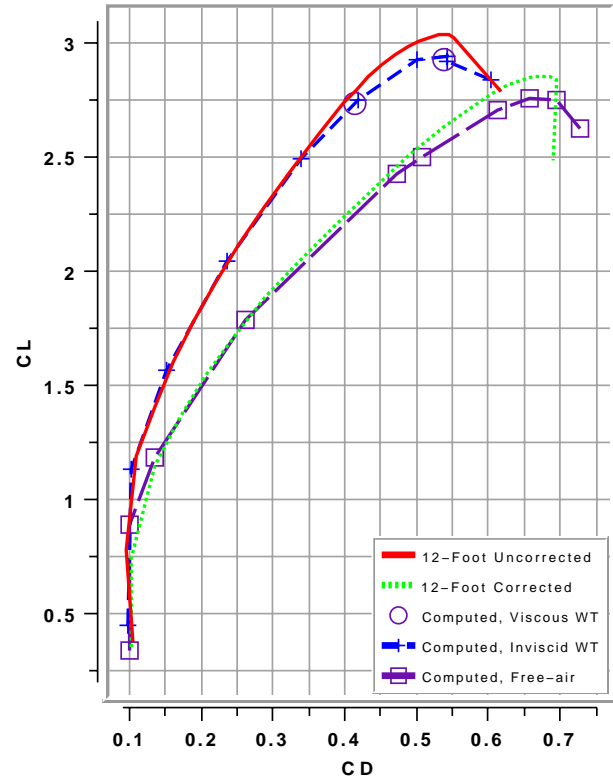


Fig. 10.  $CL$  versus  $CD$ .

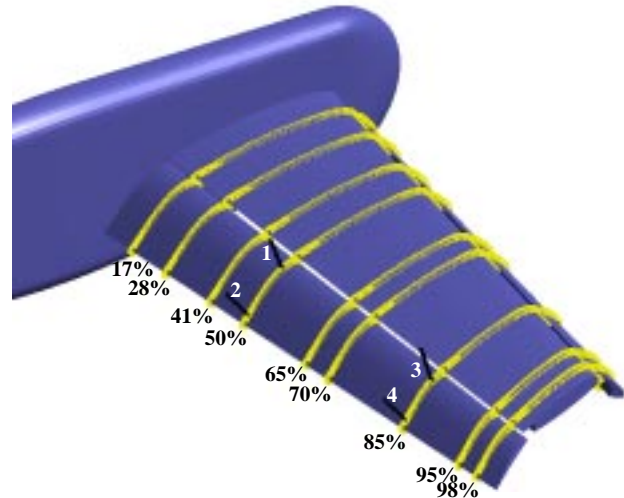


Fig. 11. Location of  $C_p$  and velocity data.

Figures 12 and 13 show a comparison of uncorrected experimental surface pressure coefficients ( $C_p$ ) with that from the computational cases using both viscous and inviscid wind-tunnel configurations at  $\alpha = 20$  and 26 degrees. The viscous-tunnel results are plotted with a solid line and the inviscid tunnel results are plotted with a dashed line; however the results are so similar that the two sets of lines are indistinguishable from



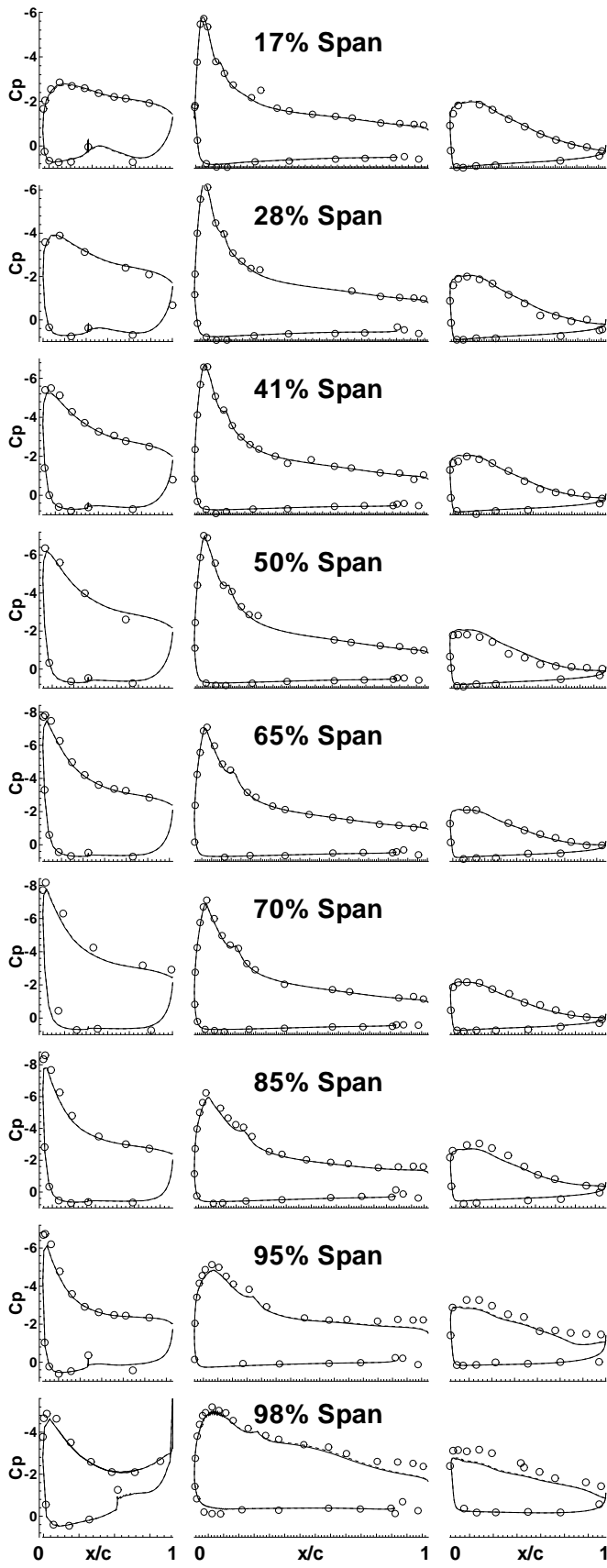


Fig. 12.  $C_p$  at  $\alpha=20$  degrees: solid line = viscous-tunnel calculations; dashed line = inviscid-tunnel calculations; circles = experiment.

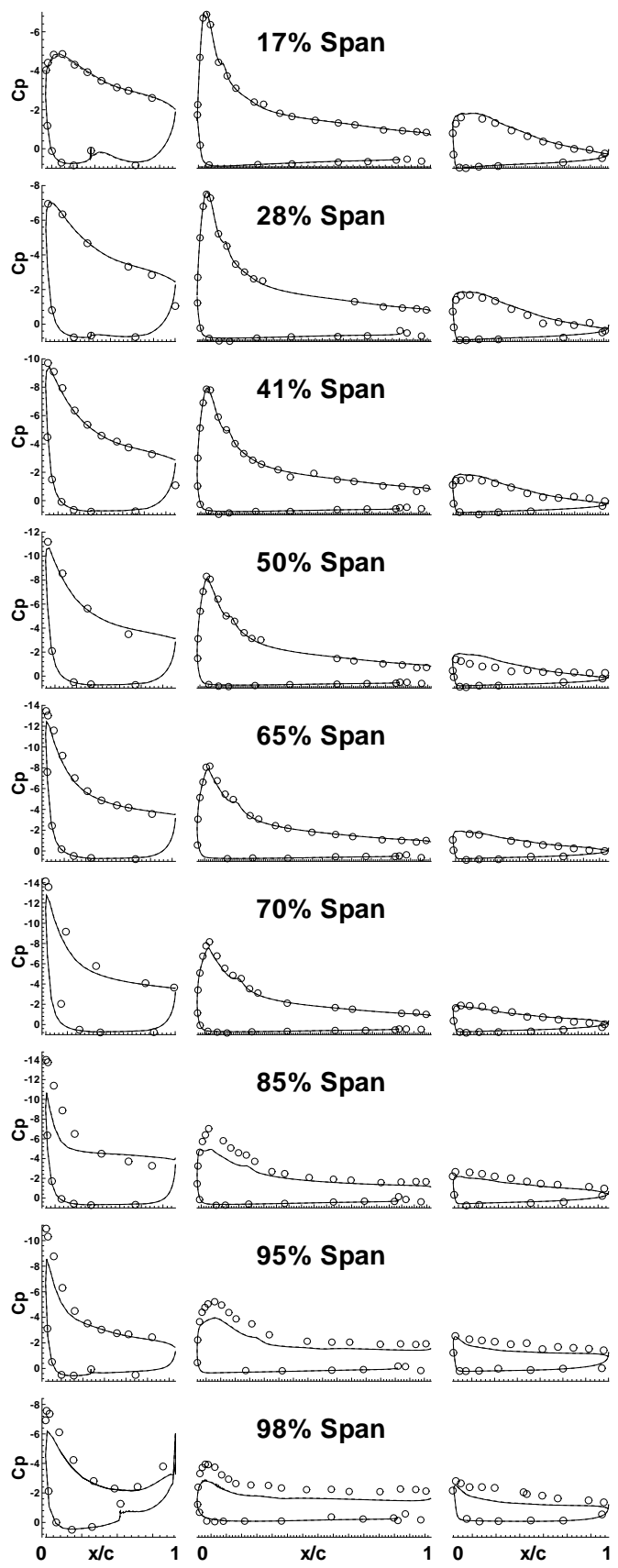


Fig. 13.  $C_p$  at  $\alpha=26$  degrees: solid line = viscous-tunnel calculations; dashed line = inviscid-tunnel calculations; circles = experiment.

each other. The agreement between the experimental data and the computational  $C_p$  is very good, especially at  $\alpha = 20$ . The computed results are producing less lift on the outboard region of the wing, particularly at  $\alpha = 26$ . Thus, the lower computed lift near  $CL_{max}$  appears to be due to a loss of lift at the outboard portion of the wing.

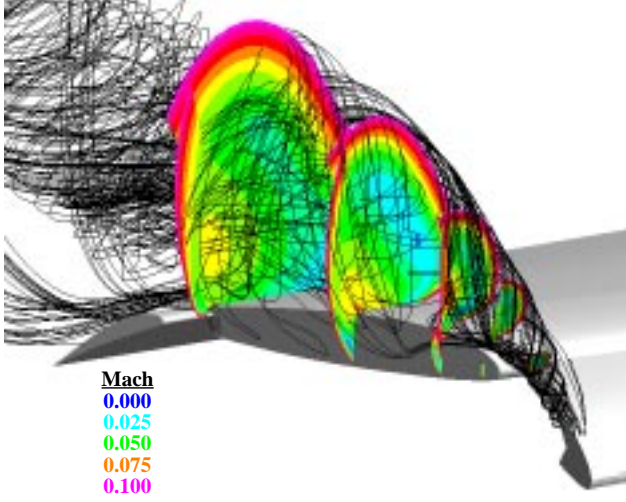


Fig. 14. Mach contours and particle traces,  $\alpha = 26$ .

Examination of the  $\alpha = 26$  inviscid-tunnel solution at the wingtip reveals a large vortex, starting at the slat edge, which convects and bursts over the top of the wing. This is shown in Fig. 14, which plots Mach-number contours and particle traces released at the slat edge. The Mach contours are drawn for values in the range between 0.0 and 0.1, and thus identify slow-moving fluid. The computed vortex spreads very rapidly as it passes over the wing, reducing the lift generated by the outboard portion of the wing. The grid resolution in the surface-normal direction has been refined enough to resolve the slat wake, but is not fine enough to properly resolve this slat-tip vortex. The spanwise resolution in this region is probably also inadequate for this purpose. Thus, to better predict  $CL_{max}$ , the grid in this region probably needs to be refined.

Figure 15 shows a comparison of the  $C_p$  data on the side wind-tunnel walls (above and below the semi-span wing) from the inviscid-tunnel computations, the viscous-tunnel computations, and the experiment, for the 26 degree angle-of-attack cases. The data are taken from the wind-tunnel walls at the 32% constant-span plane of the model. The results from the wall adjacent to the pressure side of the wing are plotted in Fig. 15a, and the suction-side wall results are shown in Fig. 15b. Very little difference is seen between the two computational results, and they both agree very well with the experimental data.

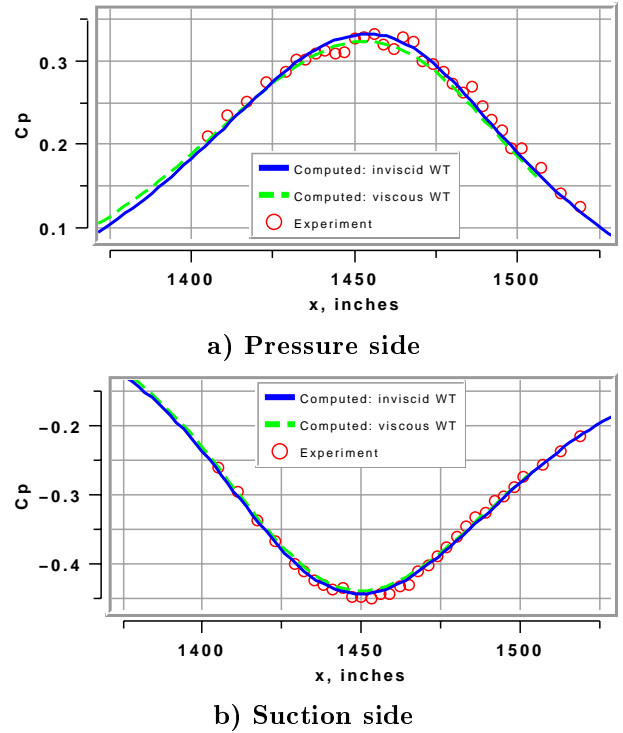
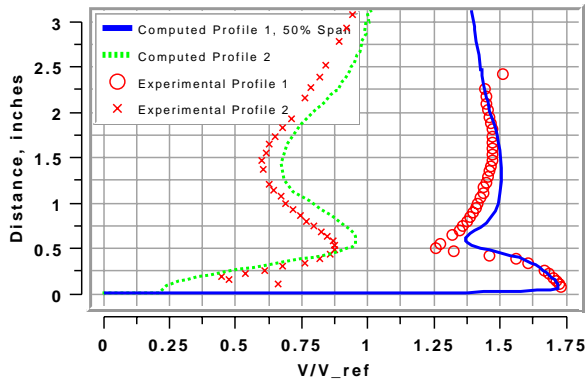
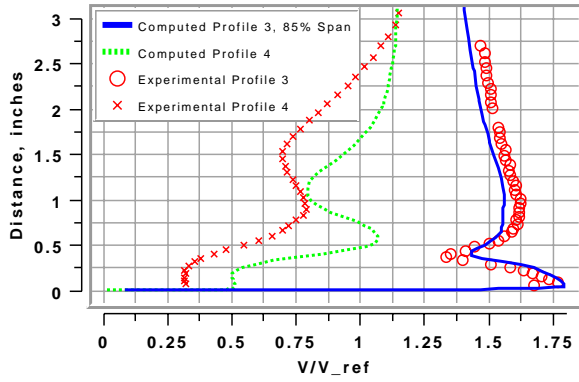


Fig. 15. Wind-tunnel wall  $C_p$  at  $\alpha = 26$ .

Figures 16, 17, and 18 present velocity-magnitude profiles for  $\alpha = 10, 20$ , and  $24$  degrees, respectively. These plots compare the computed and experimental results at the surface-normal lines drawn in Fig. 11. The  $\alpha = 20$  degree plot in Fig. 17 includes both the viscous and inviscid wind-tunnel computations, whereas the other figures show only inviscid wind-tunnel computations. There are no discernible differences between the viscous and inviscid wind-tunnel profiles. The computed profiles agree quite well with experiment at  $\alpha = 10$  degrees, although the computed profile 4 shows less deceleration and less merging of the wing wake and the flap boundary layer than the experiment. This is also evident in the subsequent plots: the computed slat and wing wakes and flap boundary layer are slower to merge together, and the experimental profiles 2 and 4 show more deceleration of the flow at the trailing edge of the flap. In fact, the experimental wing wake at  $\alpha = 24$  shows evidence of off-body separation, which does not appear to be present in the computations.

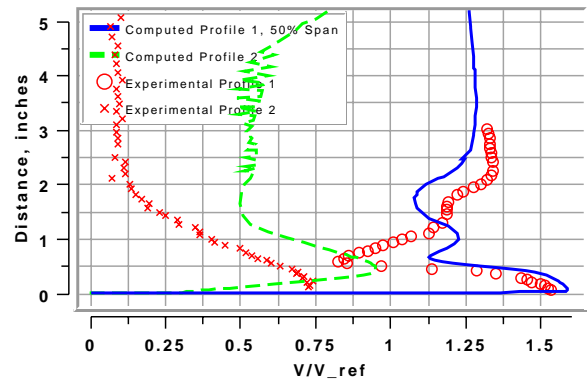


a) 50% span

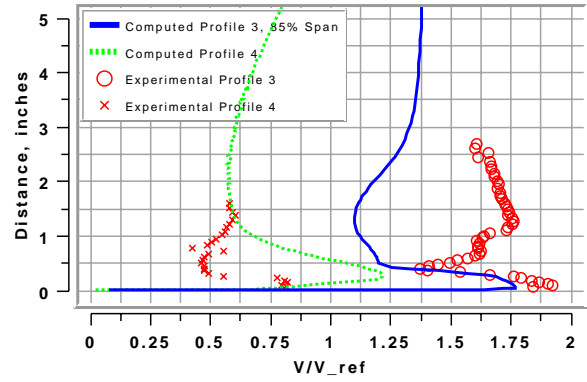


b) 85% span

Fig. 16. Velocity profiles for  $\alpha = 10$ .

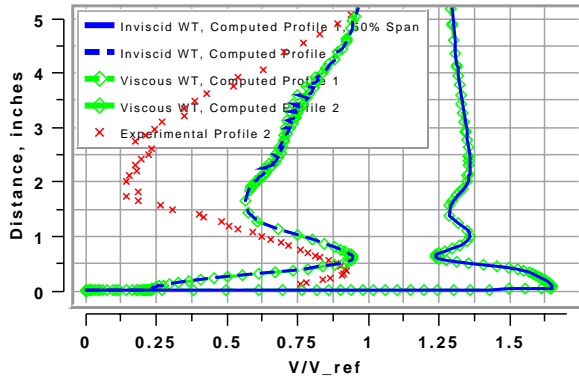


a) 50% span

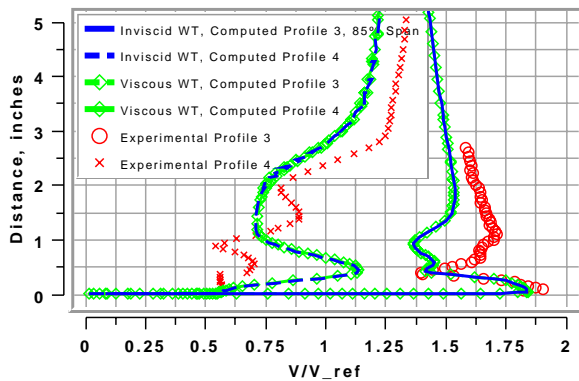


b) 85% span

Fig. 18. Velocity profiles for  $\alpha = 24$ .



a) 50% span



b) 85% span

Fig. 17. Velocity profiles for  $\alpha = 20$ .

### Wind-Tunnel Versus Free-Air

After running all of the inviscid wind-tunnel cases, an attempt was made to compute a free-air case with the same lift as one of the higher angle-of-attack wind-tunnel cases. This was done to enable a comparison of local flow quantities and thus ascertain how effective a global angle-of-attack change is for providing wind-tunnel corrections. The inviscid wind-tunnel case at  $\alpha = 16$  degrees, with a lift coefficient of 2.493, was chosen. The free-air lift curve in Fig. 9 intersects this lift level at  $\alpha = 21.46$  degrees. This free-air case was computed, and the resulting lift coefficient was 2.502, only 0.4% higher. The resulting surface pressures are plotted in Fig. 19. Also included in Fig. 19 are the experimental and inviscid wind-tunnel computational data from  $\alpha = 16$  degrees. It can be seen there are significant differences between the two computed cases. The free-air data shows more suction on the slat upper surface, and thus more lift being generated on the slat. This results in a higher suction peak on the wing leading edge, and also more down-wash on the wing, which in turn results in less lift on the wing and flap.

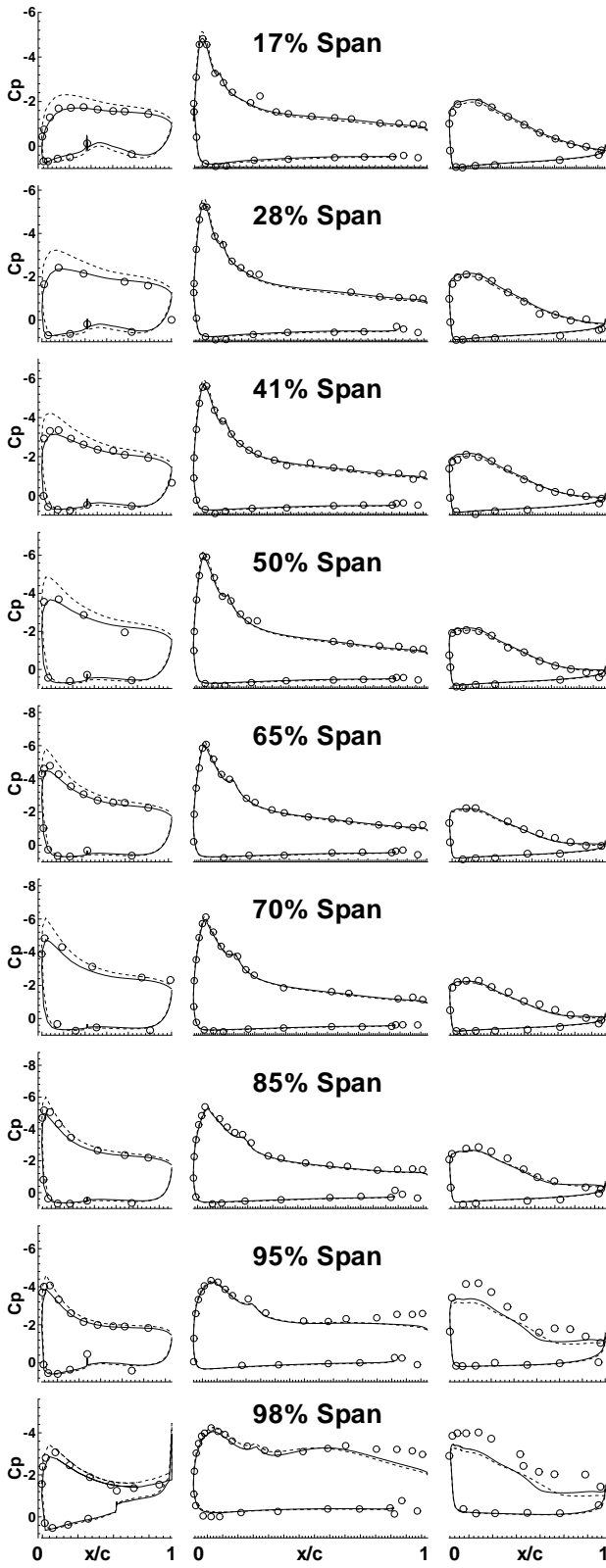


Fig. 19.  $C_p$  for wind-tunnel and free-air at  $CL = 2.5$ ; solid line = inviscid wind tunnel calculations,  $\alpha = 16^\circ$ ; dashed line = free-air calculations,  $\alpha = 21.46^\circ$ ; circles = experiment,  $\alpha = 16^\circ$ .

Thus, a global correction to the angle of attack applied to a free-air calculation can result in the same

integrated force quantities, such as lift, as computed in a wind-tunnel calculation. But the local flow quantities between the two cases may differ enough to change the relative loading of the wing elements. The conclusion is that it is always preferable to use a model of the wind-tunnel, and not free-air boundary conditions, when utilizing experimental trap-wing data from the 12-Foot.

### Grid Refinement

The next step toward validation is to understand the differences between the experimental and computational results at maximum lift conditions. The differences in  $C_p$  and the presence of the large slat-tip vortex at  $\alpha = 26^\circ$ , indicate that the spanwise grid resolution is probably not adequate outboard. To test this hypothesis, a new grid system was generated by adding 50% more spanwise grid points to the wing, slat, and flap. These new grid points were all added outboard of the 75% spanwise plane. This resulted in spanwise spacing of 0.4 inches over the outboard region of the wing components. Also, additional chord-wise grid-points were added to the slat to improve the resolution of the formation of the slat-tip vortex. The refined grid system was generated using the inviscid model of the wind tunnel, and contained 8.7 million grid points.

Solutions were computed using this new grid system for several angles of attack. The resulting lift coefficients are plotted in Fig. 20, with the results from the original inviscid wind-tunnel grid system, and the experimental results. At low angles of attack, the refined-grid results showed no change in the computed forces compared with the original computed data. However, distinct changes occur in the vicinity of maximum lift. The refined-grid  $CL_{max}$  is about 0.2 higher, and occurs at an angle of attack that is about four degrees beyond both the previous computation and the experiment.

Figure 21 plots the surface  $C_p$  comparing the new-grid results with the old-grid results and the experimental data for  $\alpha = 26^\circ$ . The largest changes in the flow are near the wing tip, as expected. The new-grid  $C_p$  show excellent agreement with the experiment; this grid refinement has clearly improved the computational results outboard. Close examination of the upper surfaces indicate slightly lower pressures in the new solution across the entire span, which is evidence of the higher lift generated in the new solution. Even though these surface pressures show better agreement with experiment than before, the refined grid is no closer to accurately predicting  $CL_{max}$ . This indicates that examination of the surface pressures alone is not enough to validate the computational ability to predict  $CL_{max}$ , and that doing so is dependent on the accuracy of the off-body viscous flow phenomena.

Figure 22 plots the velocity profiles at  $\alpha = 24$  degrees comparing the new-grid results with those from the original grid and the experiment. At the 50% span locations, the new grid results are not much different than before, except that the velocity magnitude is higher, consistent with higher lift. The 85% span profiles from the new-grid computations are quite different than the previous computations, and show fairly good agreement with experiment at profile 3. However, there are significant differences between the new results and the experiment at profile 4. In both profiles 2 and 4, the experiment shows significantly slower velocities, and possible off-body separation of the wing wake above the flap. Understanding this difference is key to understanding the differences in  $CL_{max}$ .

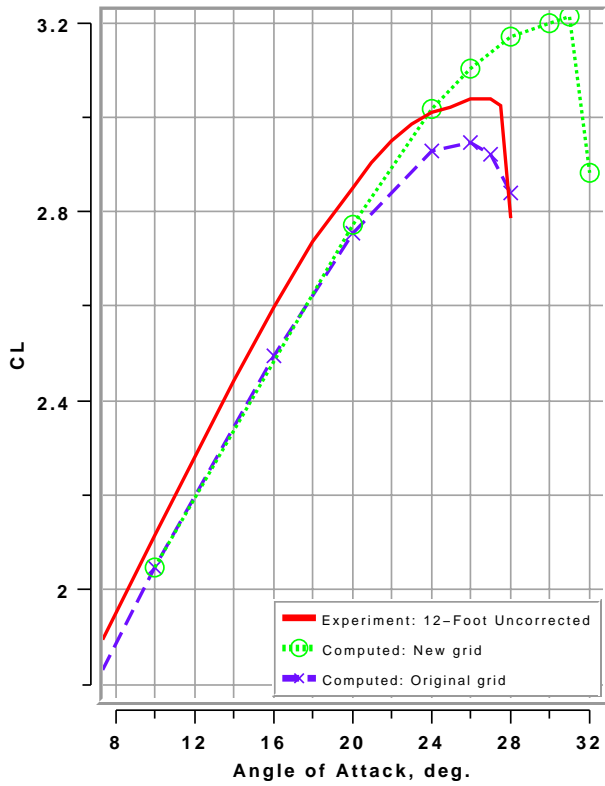


Fig. 20.  $CL$  versus  $\alpha$ .

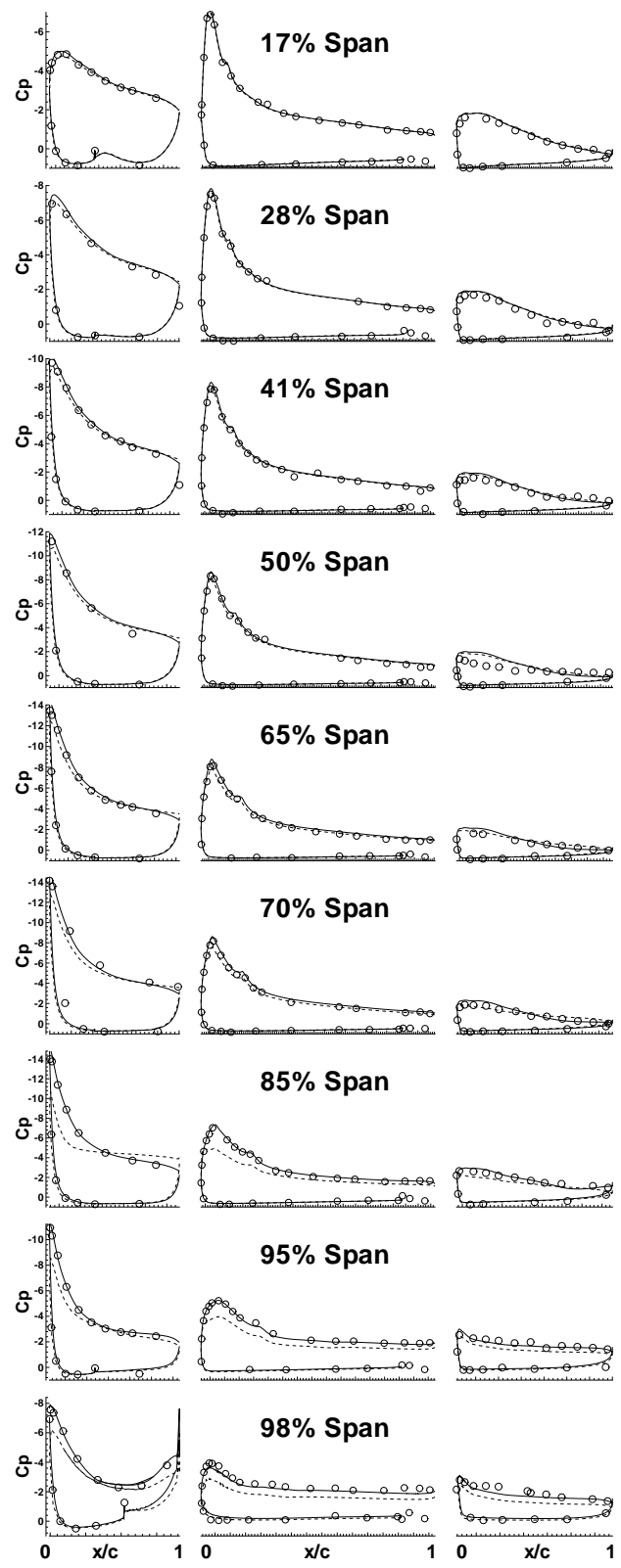
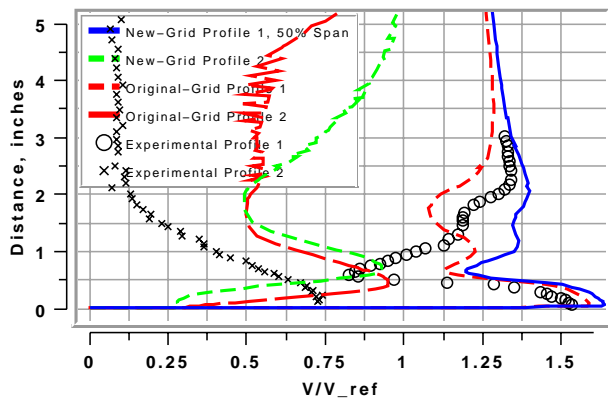
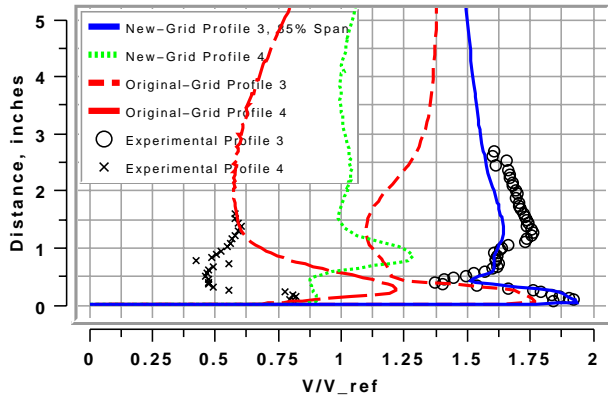


Fig. 21.  $C_p$  at  $\alpha = 26$ ; solid line = new grid; dashed line = old grid.



a) 50% span



b) 85% span

Fig. 22. Velocity profiles for  $\alpha = 24$ .

### Summary and Conclusions

Results from an attempt to validate an overset-grid approach and the OVERFLOW solver for flow over a high-lift trapezoidal wing have been presented. Computations were performed using free-air boundary conditions, a high-fidelity viscous model of the NASA Ames 12-Foot Pressure Wind Tunnel, and a simplified, inviscid model of this wind tunnel. Only very minor differences were found between the two versions of the wind-tunnel simulations. The agreement between the computational and experimental lift and surface pressures are very good at lower angles of attack, and not quite as good at higher angles of attack. The computed maximum lift was 3% lower than the experimental maximum lift. The computed velocity profiles above the flap at two spanwise stations showed some agreement at the 10 degrees angle of attack, but showed some significant differences at 20 and 24 degrees angle of attack. Investigation into the refinement of the grid system in the spanwise direction and of the slat chordwise spacing has led to improved predictions of the surface pressures at  $\alpha = 26$  degrees, and also resulted in a computed  $CL_{max}$  which was 5% higher than the experimental data.

The data presented here shows a significant amount of evidence that the inviscid-tunnel approach is as accurate at simulating the wind-tunnel interference as the significantly more complex (and more computationally expensive) viscous-tunnel approach. Comparison of the pressure coefficients from free-air and inviscid-tunnel computations at the same lift conditions indicate that it is necessary to model the tunnel in order to compare local flow quantities with the 12-Foot experimental data.

The results of the grid-refinement study indicate that not all grid sensitivities have been removed. Additional grid-refinement studies are warranted in the future. Once it has been determined that a grid-independent solution has been obtained, it would be possible to continue the validation effort by studying the effects of the modeling of transition, turbulence, and unsteady flow on the ability to compute  $CL_{max}$ . Additional assessments of the ability to predict Reynolds number effects, and the effects of flap and slat rigging changes could be performed by comparing with other configurations and conditions tested in the 12-Foot.

Despite the questions arising near maximum lift, this work has accomplished its intended goals. The results have demonstrated that the presence of the wind tunnel walls impacts the flow, and for the most accurate simulation, the facility must be included in the computational model. It has been demonstrated that the current CFD approach can predict accurate forces and surface pressures at low to moderate angles of attack.

### Acknowledgments

The authors great-fully acknowledge the technical help of Dr. Pieter Buning and Mr. Kenneth Jones of NASA Langley Research Center; of Mr. M. David Baker, Dr. Michael Olsen, and Mr. Mike Madson of NASA Ames Research Center; and of Dr. Paul Johnson of the Boeing Company. They also wish to acknowledge the helpful comments from Mr. Lyndell King and Dr. Cetin Kiris of NASA Ames Research Center in their review of this work. This work was partially funded by the Advanced Subsonic Technology Program through NASA contract NAS2-20268.

### References

- <sup>1</sup> Benek, J. A., Buning, P. G., and Steger, J. L., "A 3-D Chimera Grid Embedding Technique," AIAA Paper 85-1523, July 1985.
- <sup>2</sup> Rogers, S. E., Cao, H. V. and Su, T. Y., "Grid Generation For Complex High-Lift Configurations," AIAA Paper 98-3011, June 1998.
- <sup>3</sup> Rogers, S. E., Roth, K., Nash, S. M., Baker, M. D., Slotnick, J. P., Cao, H. V., and Whitlock,



- M., "Advances in Overset CFD Processes Applied to Subsonic High-Lift Aircraft," AIAA Paper 2000-4216, Aug. 2000.
- <sup>4</sup> Buning, P. G., Jespersen, D. C., Pulliam, T. H., Chan, W. M., Slotnick, J. P., Krist, S. E., Renze, K. J., "OVERFLOW User's Manual, Version 1.8b," NASA Langley Research Center, Hampton VA, 1998.
- <sup>5</sup> Jespersen, D. J., Pulliam, T. H., and Buning, P. G., "Recent Enhancements to OVERFLOW," AIAA Paper 97-0644, Jan. 1997.
- <sup>6</sup> Lynch, F. T., Potter, R. C., and Spaid, F. W., "Requirements for Effective High Lift CFD," ICAS Proceedings, 20th Congress, Sept. 1996.
- <sup>7</sup> Meredith, P. T., "Viscous Phenomena Affecting High-Lift Systems and Suggestions for Future CFD Development," *High-Lift System Aerodynamics*, AGARD CP-515, Paper No. 19, Sept. 1993.
- <sup>8</sup> Bussoletti, J., Johnson, P., Jones, K., Roth, K., Slotnick, J. P., Ying, S., and Rogers, S. E., "The Role of Applied CFD within the AST/IWD Program High-Lift Subelement: Applications and Requirements," AST/IWD Program Report, June 1996. To be published as a NASA TM.
- <sup>9</sup> Mathias, D. L., Roth, K., Ross, J. C., Rogers, S. E., Cummings, R. M., "Navier-Stokes Analysis of the Flow about a Flap-Edge," AIAA Paper 95-0185, Jan. 1995.
- <sup>10</sup> Jones, K. M., Biedron, R. T., and Whitlock, M., "Application of a Navier-Stokes Solver to the Analysis of Multielement Airfoils and Wings Using Multizonal Grid Techniques," AIAA Paper 95-1855, June 1995.
- <sup>11</sup> Cao, H. V., Rogers, S. E., and Su, T. Y., "Navier-Stokes Analyses of a 747 High-Lift Configuration," AIAA Paper 98-2623, June 1998.
- <sup>12</sup> Mavriplis, D. J., "Large-Scale Parallel Unstructured Mesh Computations for 3D High-Lift Analysis," AIAA Paper 99-0537, January 1999.
- <sup>13</sup> Mavriplis, D. J., "Three-Dimensional Viscous Flow Analysis for High-Lift Configurations Using a Parallel Unstructured Multigrid Solver" SAE Paper No. 1999-01-5558, October 1999.
- <sup>14</sup> Nash, S. M. and Rogers, S. E., "Numerical Study of a Trapezoidal Wing High-Lift Configuration," SAE Paper No. 1999-01-5559, October 1999.
- <sup>15</sup> Slotnick, J. P., An, M. Y., Mysko, S. J., Yeh, D. T., Rogers, S. E., Roth, K., Baker, M. D., and Nash, S. M., "Navier-Stokes Analysis of a High-Wing Transport High-Lift Configuration with Externally Blown Flaps," AIAA Paper 2000-4219, Aug. 2000.
- <sup>16</sup> Rogers, S. E., Roth, K., Slotnick, J. P., Cao, H. V., Whitlock, M., Nash, S. M., and Baker, M. D., "Computation of Viscous Flow For a Boeing 777 Aircraft in Landing Configuration," AIAA Paper 2000-4221, Aug. 2000.
- <sup>17</sup> Johnson, P., Jones, K. M., and Madson, M., "Experimental Investigation of a Simplified 3D High Lift Configuration in Support of CFD Validation," AIAA Paper 2000-4217, Aug. 2000.
- <sup>18</sup> King, L. S. and Johnson, D. A., "Transonic Airfoil Calculations Including Wind Tunnel Wall-Interference Effects," AIAA J., Vol. 24, No. 8, Aug. 1986.
- <sup>19</sup> Beutner, T. J., "A Method for the Modelling of Porous and Solid Wind Tunnel Walls in Computational Fluid Dynamics Codes," Ph.D. Dissertation, Stanford University, Dec. 1993.
- <sup>20</sup> Martin, F. W., Sickles, W. L., and Stanley, S. A., "Transonic Wind Tunnel Wall Interference Analysis for the Space Shuttle Launch Vehicle," AIAA Paper 93-0420, Jan. 1993.
- <sup>21</sup> Vatsa, V. N. and Wedan, B. W., "Navier-Stokes Solutions for Transonic Flow Over a Wing Mounted in a Tunnel," AIAA Paper 88-0102, Jan. 1988.
- <sup>22</sup> Cao, H. V., Kusunose, K., Spalart, P., Ishimitsu, K., Rogers, S. E., and McGhee, R., "Study of Wind Tunnel Wall Interference for Multi-Element Airfoils Using a Navier-Stokes Code," AIAA Paper 94-1933, June 1994.
- <sup>23</sup> Djomehri, M. J., "CFD Modeling of the 12-Foot Pressure Wind Tunnel," Calspan Internal Report, NASA Ames Research Center, Apr. 1996.
- <sup>24</sup> Chan, W. M., Rogers, S. E., Nash, S. M., and Buning, P. G.: Chimera Grid Tools, Version 1.1 User Guide, NASA Ames Research Center, Moffett Field, CA, Oct. 1998. <http://george.arc.nasa.gov/~srogers/cgt/doc/man.html>
- <sup>25</sup> Parks, S. J., Buning, P. G., Steger, J. L., and Chan, W. M., "Collar Grids for Intersecting Geometric Components within the Chimera Overlapped Grid Scheme," AIAA Paper 91-1587, July 1991.
- <sup>26</sup> Taft, J., "OVERFLOW Gets Excellent Results on SGI Origin2000," *NAS News*, Vol. 3, No. 1, Jan. 1998. <http://www.nas.nasa.gov/Pubs/NASnews/98/01/overflow.html>
- <sup>27</sup> Jespersen, D. J., "Parallelism and OVERFLOW," NAS Technical Report NAS-98-013, October 1998. <http://www.nas.nasa.gov/Pubs/TechReports/NASreports/NAS-98-013/>
- <sup>28</sup> Roe, P. L., "Approximate Riemann Solvers, Parameter Vectors, and Difference Schemes," *J. Comput. Phys.*, Vol. 43, pp. 357-372, 1981.
- <sup>29</sup> Spalart, P. R. and Allmaras, S. R., "A One-Equation Turbulence Model for Aerodynamic Flows," AIAA Paper 92-0439, Jan. 1992.